Rotationally Commensurate Growth of MoS$_2$ on Epitaxial Graphene
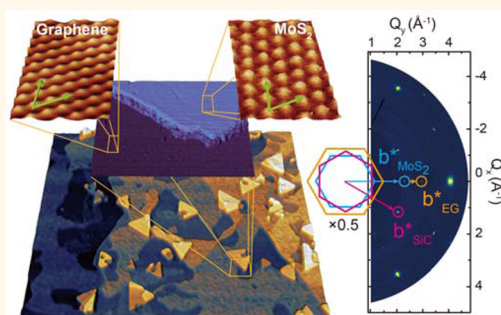
Xiaolong Liu,[†,¶] Itamar Balla,[‡,¶] Hadallia Bergeron,[‡] Gavin P. Campbell,[‡] Michael J. Bedzyk,*[,†,‡,§] and Mark C. Hersam*[,†,‡,‖,⊥]

[†]Graduate Program in Applied Physics, [‡]Department of Materials Science and Engineering, [§]Department of Physics, [‖]Department of Chemistry, and [⊥]Department of Medicine, Northwestern University, Evanston, Illinois 60208, United States

Ⓢ *Supporting Information*

ABSTRACT: Atomically thin MoS$_2$/graphene heterostructures are promising candidates for nanoelectronic and optoelectronic technologies. Among different graphene substrates, epitaxial graphene (EG) on SiC provides several potential advantages for such heterostructures, including high electronic quality, tunable substrate coupling, wafer-scale processability, and crystalline ordering that can template commensurate growth. Exploiting these attributes, we demonstrate here the thickness-controlled van der Waals epitaxial growth of MoS$_2$ on EG *via* chemical vapor deposition, giving rise to transfer-free synthesis of a two-dimensional heterostructure with registry between its constituent materials. The rotational commensurability observed between the MoS$_2$ and EG is driven by the energetically favorable alignment of their respective lattices and results in nearly strain-free MoS$_2$, as evidenced by synchrotron X-ray scattering and atomic-resolution scanning tunneling microscopy (STM). The electronic nature of the MoS$_2$/EG heterostructure is elucidated with STM and scanning tunneling spectroscopy, which reveals bias-dependent apparent thickness, band bending, and a reduced band gap of ~0.4 eV at the monolayer MoS$_2$ edges.

KEYWORDS: *transition metal dichalcogenide, silicon carbide, scanning tunneling microscopy, synchrotron X-ray scattering, chemical vapor deposition, van der Waals heterostructure*

Vertical heterostructures composed of stacked two-dimensional (2D) materials allow the exploration of fundamental interfacial interactions and novel electronic functionality. From among the 2D material library consisting of semimetals (*e.g.*, graphene[1,2]), insulators (*e.g.*, boron nitride[3] and Bi$_2$Se$_3$[4]), and semiconductors (*e.g.*, black phosphorus[5−7] and transition metal dichalcogenides[8,9]), the MoS$_2$/graphene heterostructure[10,11] shows great potential for next generation electronic and optoelectronic applications due to complementary carrier mobilities and optical responsivities.[12] Additionally, the MoS$_2$/graphene heterostructure has been shown to be an excellent catalyst for hydrogen evolution reactions[13] and a promising anode material for Li-ion batteries.[14]

The properties of MoS$_2$/graphene heterostructures depend strongly on the underlying substrate and the graphene synthesis technique. Epitaxial graphene (EG) grown on SiC by the preferential thermal desorption[15,16] of silicon from SiC not only offers uniform large-area synthesis of graphene but also provides technological advantages over alternative methods such as chemical vapor deposition (CVD) and mechanical exfoliation. For example, fine control of the growth temperature enables homogeneous monolayer or bilayer EG at the wafer scale,[17−19] while postannealing in hydrogen allows decoupling

of EG from the underlying SiC substrate.[2] The high quality and cleanliness of EG is evidenced by its high carrier mobility[20] of 45 000 cm^2 V^{-1} s^{-1} and observation of the quantum Hall effect.[21] Furthermore, the interaction between graphene and the SiC substrate can be tailored *via* intercalation of different atomic species.[22]

Given the underlying SiC substrate as well as the different electronic characteristics of EG (*e.g.*, substrate-induced n-type doping[23,24]), CVD synthesis of MoS$_2$ on EG is expected to differ from that on graphite or CVD graphene, giving rise to novel structural and electronic interactions between the two materials. While MoSe$_2$ has been grown on EG by molecular beam epitaxy,[25,26] recent reports of MoS$_2$ grown by CVD on graphite[9,27,28] and EG[29,30] resulted in non-epitaxial growth, where the orientation of the MoS$_2$ crystals was not controlled. Furthermore, the atomic-scale electronic and structural properties of MoS$_2$/EG heterostructures have not been thoroughly established. Toward these ends, we report here the rotationally commensurate growth of atomically thin MoS$_2$ crystals on EG
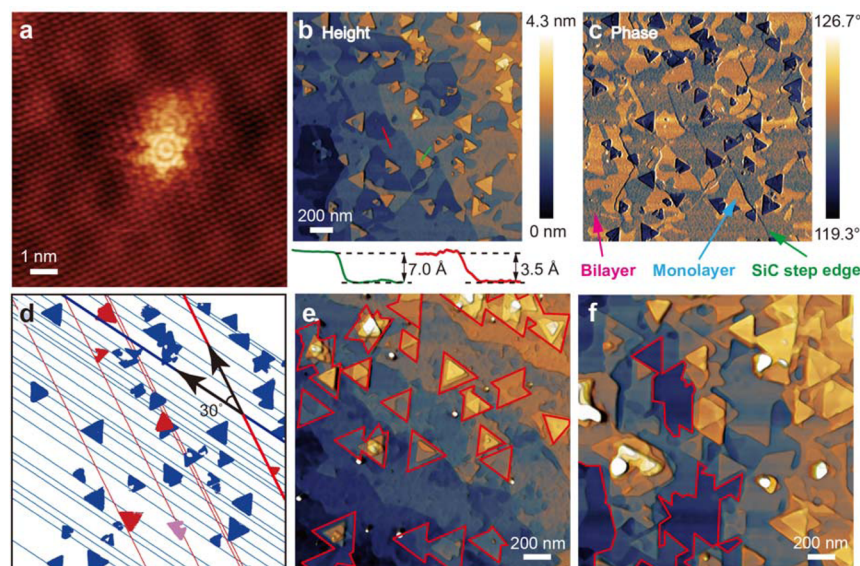
Figure 1. CVD-grown MoS$_2$ on EG at different conditions. (a) UHV STM image of EG before growth of MoS$_2$, showing a typical rotational grain boundary on EG (V_{sample} = −0.1 V, $I_{tunneling}$ = 0.4 nA). EG lattice and underlying SiC $(6\sqrt{3} \times 6\sqrt{3})R30°$ reconstruction are clearly observed. (b) AFM height and (c) phase images of MoS$_2$/EG grown at 43 Torr. Line profiles show monolayer MoS$_2$ (green) and graphene (red) thicknesses. The contrast between bilayer and monolayer regions of EG is more obvious in the phase image. (d) Extraction of edge orientations of MoS$_2$ crystals in (b), showing two predominant registrations of MoS$_2$ on EG. (e) AFM images of MoS$_2$/EG grown at 50 Torr and (f) 100 Torr, showing multilayer growth and larger crystal domain size. The interface between EG and MoS$_2$ is highlighted in red.

by van der Waals epitaxy. We investigate the electronic and structural properties of the resulting MoS$_2$/EG heterostructures by a comprehensive suite of methods including atomic force microscopy (AFM), ultrahigh vacuum (UHV) scanning tunneling microscopy and spectroscopy (STM/STS), synchrotron X-ray scattering, *in situ* X-ray photoelectron spectroscopy (XPS), and Raman spectroscopy. In addition to the inherent advantages of van der Waals epitaxy (*e.g.*, reduced defect density,[31] sharper interfaces,[32] and consistent material quality), the registry between the MoS$_2$ and EG allows for the study of crystal orientation-dependent properties (*e.g.*, anisotropic thermal conductance of MoS$_2$[33]) and specific types of grain boundaries (*e.g.*, mirror twin grain boundaries[34]) for fundamental studies[34] and electronic applications.[35] Specifically, the epitaxial growth of MoS$_2$ hinders the formation of tilt grain boundaries that degrade in-plane electrical conductivity and favors the formation of mirror twin grain boundaries that preserve in-plane electrical conductivity.[34] It has also been demonstrated that the type of grain boundary affects the optical properties of MoS$_2$.[34] Therefore, the ability to synthesize rotationally commensurate MoS$_2$ domains on EG facilitates ongoing efforts to realize reproducibly high-performance MoS$_2$/graphene electronic and optoelectronic devices.

RESULTS AND DISCUSSION

CVD growth of MoS$_2$ on EG is performed at a variety of conditions in order to tune and optimize the MoS$_2$ film thickness. Figure 1a is an STM image of EG prior to MoS$_2$ growth that contains a rotational grain boundary on EG with atomic structure consistent with that in previous literature.[36,37] In addition to the rotational grain boundary defect, the graphene lattice and underlying $(6\sqrt{3} \times 6\sqrt{3})R30°$ SiC reconstruction are clearly resolved. Figure 1b,c shows the AFM topography and phase images, respectively, of MoS$_2$ grown on EG at 43 Torr (detailed growth conditions are given in Methods; additional AFM images are provided in Figure S1).

The measured thickness of a MoS$_2$ triangular domain is 7.0 Å, as indicated by the green line profile in Figure 1b, corresponding to monolayer MoS$_2$.[38] Monolayer and bilayer graphene regions are observed in the topography image (Figure 1b) and are more clearly distinguished in the phase image (Figure 1c), where monolayer regions are brighter. The measured step height is 3.5 Å, as indicated by the red line profile in Figure 1b, which is also in agreement with the literature.[39] Figure 1d extracts the edge orientations of the MoS$_2$ triangles shown in Figure 1b by plotting a line along one edge of each triangle. A large majority of the triangles have parallel edges as indicated by the blue lines, while a few triangles, indicated in red, have edges rotated by 30°. The rare occurrence of a third rotational orientation of a MoS$_2$ triangular domain is shown in pink. From this analysis, it is apparent that there are two predominant types of azimuthal registration of MoS$_2$ on EG. This crystal orientation alignment is attributed to van der Waals epitaxy,[32] which accommodates the large lattice mismatch (~28%) between graphene and MoS$_2$, as will be further discussed below.

Examination of the growth nucleation sites reveals that MoS$_2$ growth preferentially (but not exclusively) initiates at the step edges of the underlying SiC and graphene. This observation can be explained by the higher reactivity of graphene as a function of local curvature[40,41] at SiC steps and exposed graphene edges.[42] Indeed, STS spatial maps reveal different electronic properties of the graphene wrinkles and edges compared to the flat regions, as shown in Figure S2. Higher growth pressures of 50 and 100 Torr result in bilayer and pyramid-like multilayer growth with larger domain sizes and higher coverage, as shown in Figure 1e,f, respectively, where the interface between EG and MoS$_2$ is highlighted in red. Higher synthesis pressure increases the local concentration of growth precursors and facilitates growth on the MoS$_2$ basal planes, resulting in multilayer crystals.[43,44] Hence, by tuning the growth pressure, the thickness of the MoS$_2$ domains can be controlled.
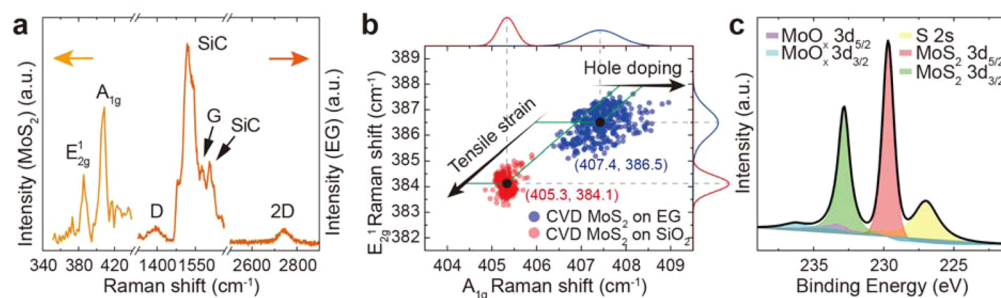
Figure 2. Raman and XPS characterization of a MoS$_2$/EG heterostructure with primarily monolayer MoS$_2$. (a) Raman spectrum of MoS$_2$/EG showing the E$_{2g}^1$ and A$_{1g}$ peaks of MoS$_2$, and the D, G, and 2D peaks of EG. (b) Strain and doping analysis of CVD MoS$_2$ on EG in comparison to CVD MoS$_2$ on SiO$_2$ from spatial Raman mapping measurements. (c) *In situ* XPS spectrum of MoS$_2$/EG after annealing at 205 °C for 6 h in UHV, showing characteristic Mo 3d doublets and minimal MoO$_x$ peaks.

The as-grown MoS$_2$/EG heterostructure is characterized by Raman spectroscopy as shown in Figure 2a. Raman signatures of MoS$_2$ (A$_{1g}$ at 407.2 cm^{-1}, E$_{2g}^1$ at 386.4 cm^{-1}) and graphene (D at 1391.2 cm^{-1}, G at 1575.4 cm^{-1}, 2D at 2740.8 cm^{-1}) are clearly resolved. Several factors affect the positions of the A$_{1g}$ and E$_{2g}^1$ modes, including layer number,[45] strain,[46] and doping.[47] Using a method previously demonstrated on graphene,[48] the strain and doping effects of MoS$_2$ on EG can be deconvolved. For this analysis, a sample of CVD-grown MoS$_2$ on SiO$_2$ was prepared (see the optical microscopy and AFM images in Figure S3). To circumvent the MoS$_2$ thickness effects on the Raman peak positions, the two samples were prepared under growth conditions that yield primarily MoS$_2$ monolayers. Spatial Raman mapping of the MoS$_2$/EG and MoS$_2$/SiO$_2$ samples was then performed, and the E$_{2g}^1$ *versus* A$_{1g}$ mode positions are plotted in Figure 2b. It has been shown previously that A$_{1g}$ and E$_{2g}^1$ modes shift up with compressive strain[46] and down with tensile strain.[49,50] Since the reported ratio of the shifting rates of E$_{2g}^1$ to A$_{1g}$ under biaxial strain is ~1.5[46] and hole doping shifts up the A$_{1g}$ mode while the E$_{2g}^1$ mode remains unchanged,[47] pure strain and doping effects are represented by two arrowed lines with slopes of 1.5 and 0 in Figure 2b, respectively. Thus, in comparison to MoS$_2$ on SiO$_2$, MoS$_2$ grown on EG has higher hole doping and lower tensile strain. The higher hole doping level may be due to differences in charge transfer for the two systems.[51,52] In addition, the lower tensile strain can be explained by the fact that while MoS$_2$/SiO$_2$ is under tensile strain,[53] MoS$_2$/EG is strain-free as will be demonstrated later by X-ray scattering. Given that the difference in the E$_{2g}^1$ mode positions between the two systems is 2.4 cm^{-1}, the corresponding tensile strain of MoS$_2$/SiO$_2$ is ~0.2%.[46]

The electronic properties of the MoS$_2$/EG heterostructure are further explored using a custom-designed UHV STM with a base pressure of ~6 × 10^{-11} Torr at room temperature.[54] Prior to scanning, the sample is degassed at 205 °C for 6 h in UHV and then characterized by *in situ* XPS. The molybdenum core level XPS spectrum is shown in Figure 2c, with detailed subpeak positions provided in the Methods section. The doublets of the Mo 3d orbital corresponding to MoS$_2$ are considerably higher than those of MoO$_x$, indicating the high quality of the MoS$_2$ crystals. Figure 3a is an STM image showing a typical monolayer MoS$_2$ crystal on EG. The (6$\sqrt{3}$ × 6$\sqrt{3}$)R30° reconstruction of EG is seen in the bottom half of the image. Nine STS spectra taken at different positions on the MoS$_2$ crystal far from its edges are shown in Figure 3b. The band gap is uniformly ~2 eV across a single domain, which falls
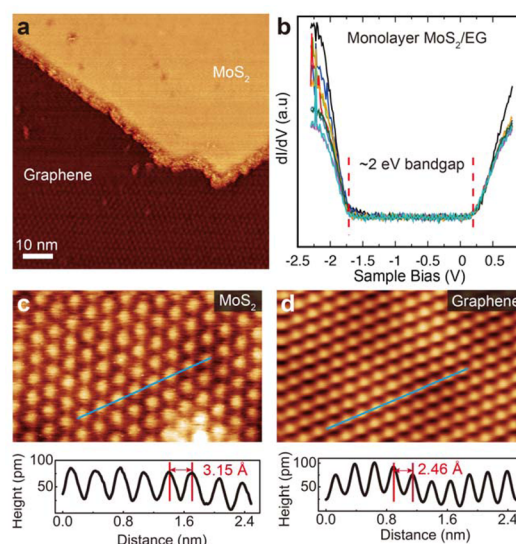

Figure 3. UHV STM/STS characterization of MoS$_2$/EG. (a) STM image of the corner of a monolayer MoS$_2$ crystal domain on EG, where the underlying SiC (6$\sqrt{3}$ × 6$\sqrt{3}$)R30° reconstruction is seen at the bottom (V_{sample} = 0.2 V, $I_{tunneling}$ = 50 pA). (b) STS dI/dV spectra taken at nine different positions on the MoS$_2$ crystal domain far away from the edges, showing a uniform band gap of ~2 eV. (c,d) Atomic-scale images and line profiles of (c) MoS$_2$ (V_{sample} = −0.2 V, $I_{tunneling}$ = 50 pA) and (d) EG (V_{sample} = −0.1 V, $I_{tunneling}$ = 0.4 nA), demonstrating aligned lattice orientations.

within the range of reported STS band gaps of monolayer MoS$_2$ on graphite (1.9 eV,[28] 2.15 eV,[9] and 2.4 eV[27]). Thermal broadening and energy uncertainty resulting from the small tunneling junction may explain the small deviations in the STS-measured band gap.[55] Atomic resolution images of a MoS$_2$ triangular domain and EG in Figure 3a are shown in Figure 3c,d, respectively. From the line profiles, the periods of atomic corrugation for MoS$_2$ and EG are measured to be 3.15 and 2.46 Å, corresponding to their respective lattice constants. Both the MoS$_2$ and EG atomic-scale STM images show six-fold symmetry and rotational commensurability as a result of van der Waals epitaxy. Figure 4a contains STS mappings of the corner of a MoS$_2$ triangle overlaid on three-dimensionally rendered STM height images taken at V_{sample} = −0.3 V and V_{sample} = 0.3 V. Since the differential tunneling conductance measured by STS is proportional to the sample density of states (DOS), the semiconducting nature of MoS$_2$ and semimetallic
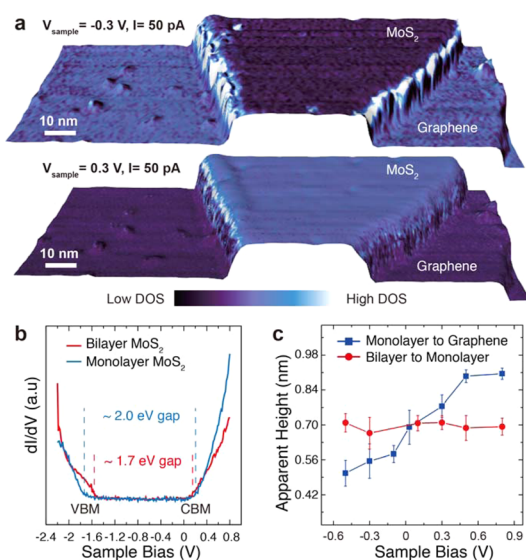
Figure 4. Electronic structure of MoS$_2$/EG. (a) STS mappings overlaid on three-dimensionally rendered topography images of MoS$_2$/EG at sample biases of −0.3 and +0.3 V, showing different relative DOS between MoS$_2$ and EG. (b) STS spectra taken on monolayer and bilayer MoS$_2$, showing a smaller band gap of ~1.7 eV for bilayer MoS$_2$. (c) Bias-dependent apparent thickness of monolayer MoS$_2$ on EG and apparent height of a monolayer to bilayer MoS$_2$ step edge.

nature of EG give rise to the inversion of the relative DOS at these two biases.

STS spectra for monolayer and bilayer MoS$_2$ are shown in Figure 4b. Compared to monolayer, bilayer MoS$_2$ has a reduced band gap of ~1.7 eV, resulting from an increased valence band maximum (VBM) and a subtle decrease of the conduction band minimum (CBM). Although the physical thickness of monolayer MoS$_2$ is ~7 Å, the apparent height measured by STM depends on applied bias, as indicated by the blue curve in Figure 4c. This convolution of topography and electronic structure in constant current STM imaging is well-known and often pronounced for ultrathin films.[56] Qualitatively, at high positive bias, the MoS$_2$ conduction band shows higher DOS

than EG, as shown in Figure 4a, which implies that the tip retracts more on MoS$_2$ than EG to maintain a constant current. On the other hand, at low negative bias, the opposite occurs as EG shows higher DOS than MoS$_2$ (Figure 4a). This change in relative DOS and the proximity of the MoS$_2$ CBM to zero makes the MoS$_2$ apparent thickness larger at high positive bias and smaller at negative bias than its physical thickness. Also shown in Figure 4c is the measured apparent height of the step edge from bilayer to monolayer MoS$_2$ at different sample biases. Since bilayer and monolayer MoS$_2$ have similar DOS in the measured range, the apparent thickness does not vary significantly from its physical thickness.

The effects of edges[57,58] on the electronic properties of MoS$_2$ are also investigated by spatially resolved STS spectra. A series of vertically offset STS spectra taken across an EG to MoS$_2$ step edge are shown in Figure 5a, with their respective positions marked by colored dots in the inset. The distance from each measured point to the step edge is further indicated in the figure. These spectra reveal that the band gap increases gradually to ~2 eV after moving ~5 nm into the MoS$_2$ flake. The dashed black lines denote the VBM and CBM of each spectrum. Both band edges shift to higher energy when approaching the MoS$_2$ edge from the interior, similar to the band bending observed for MoS$_2$ on graphite.[9] However, the gradual decrease of the band gap (*i.e.*, faster increase of the VBM than the CBM) when approaching the MoS$_2$ edge differs from the nearly constant band gap observed in the band bending region of MoS$_2$ on graphite.[9] Similar STS spectra taken across the transition from bilayer to monolayer MoS$_2$ are shown in Figure 5b. In this case, the band gap changes from ~1.7 eV on bilayer MoS$_2$ to ~2.0 eV on monolayer MoS$_2$. However, at the edge position, the band gap drops significantly to ~0.4 eV. This large decrease in the band gap is consistent with edge states[58] that have been predicted by density functional theory (DFT) to reduce the band gap of MoS$_2$ to 0.43 eV at the monolayer to bilayer step edge[59] and below 0.6 eV at isolated MoS$_2$ monolayer edges.[57]

To verify that these local AFM and STM observations persist over the entire sample, synchrotron grazing-incidence wide-angle X-ray scattering (GIWAXS) is employed to investigate the van der Waals epitaxy of MoS$_2$ on EG. A schematic of
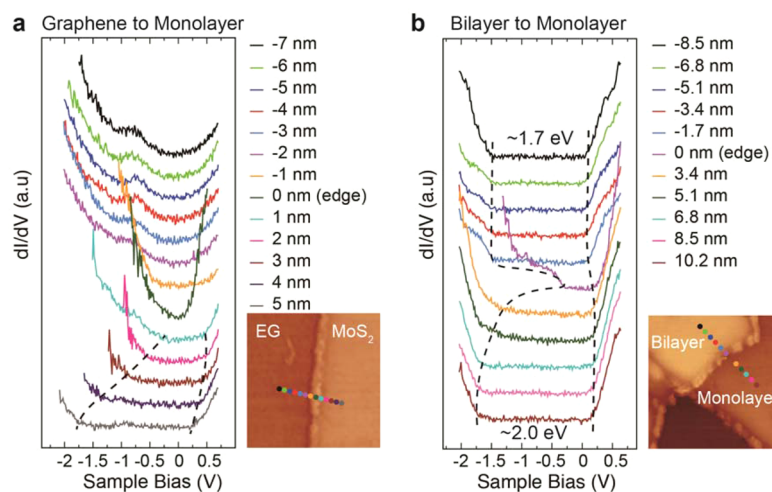

Figure 5. STS line scans across MoS$_2$ edges. (a) STS spectra taken across a monolayer MoS$_2$ edge from EG. (b) STS spectra taken across a step edge from bilayer to monolayer MoS$_2$, showing band bending and decreased band gap near the edge to ~0.4 eV.
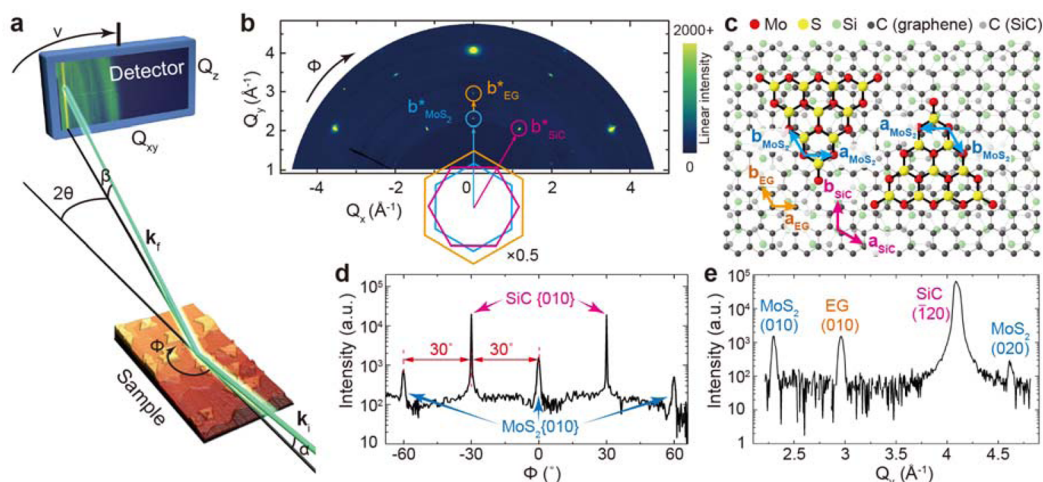
Figure 6. Rotationally commensurate van der Waals epitaxy of MoS_2 on EG. (a) Schematic of GIWAXS measurement: k_i, incident wave vector; k_f, scattering wave vector; α, incident angle; β, out-of-plane angle; 2θ, in-plane angle; φ, sample rotation angle; ν, detector rotation angle. (b) Q_{xy} 2D reciprocal space map of MoS_2/EG projected from $Q_z = 0.08$ to 0.12 Å^{-1} by synchrotron GIWAXS. The b* reciprocal space vectors are indicated by arrows. (c) Real-space model of the MoS_2/EG heterostructure with MoS_2 lattice aligned with that of EG. (d) Projected first-order peaks of MoS_2 and SiC onto ϕ, showing sharp distributions. (e) Referring to (b), in-plane scattered intensity along the Q_y direction at $Q_x = 0$. The determined real-space lattice constants of MoS_2, EG, and SiC are 3.16 ± 0.01, 2.46 ± 0.01, and 3.07 ± 0.01 Å, respectively.

GIWAXS is shown in Figure 6a, and experimental details are outlined in the Methods section. In GIWAXS, the incident X-ray beam is at an incident angle of $\alpha = 0.14°$, slightly below the critical angle of total external reflection of the substrate. The out-of-plane angle β and in-plane angle 2θ define the position at which the scattered X-ray wave vector k_f intersects the plane of the 2D detector. The Q_{xy} 2D reciprocal space map of the MoS_2/EG/SiC structure projected from $Q_z = 0.08$ to 0.12 Å^{-1} is shown in Figure 6b, with first-order spots of MoS_2, EG, and SiC identified. The blue, orange, and magenta arrows indicate the reciprocal lattice vectors b* for MoS_2, EG, and SiC, respectively. As seen by the reciprocal space points, the reciprocal lattices for MoS_2 and EG are aligned, whereas SiC has a well-known 30° rotation with respect to EG.[60] This observation indicates that the majority of the MoS_2 crystals are epitaxially grown along the EG lattice direction with matching six-fold symmetry, confirming the symmetry inferred from AFM (Figure 1 and Figure S1) and STM (Figure 3). The real-space structure reconstructed for such aligned MoS_2 growth is shown in Figure 6c, where the two MoS_2 triangles represent the preferred orientations in the epitaxial MoS_2/EG heterostructure shown in Figure 3c,d. Projected first-order MoS_2 and SiC peaks onto ϕ are included in Figure 6d to examine the angular distribution. The relative angle between the MoS_2 and SiC lattices is indeed $30 \pm 0.3°$, which is a much narrower azimuthal distribution than that of CVD MoS_2 grown on sapphire.[61] The full width at half-maxima of the first-order MoS_2, EG, and SiC peaks as a function of ϕ are 0.7, 0.5, and 0.05° (limited by X-ray optics), respectively, which confirms that the MoS_2 is in excellent registry with EG.

Figure 6e shows the scattered intensity from the 2D reciprocal space map of Figure 6b collected along Q_y at $Q_x = 0$. The real-space lattice constants calculated for MoS_2, EG, and SiC are 3.16 ± 0.01, 2.46 ± 0.01, and 3.07 ± 0.01 Å, respectively. To gain more insight into the structure of MoS_2 on EG, in-plane X-ray diffraction of MoS_2/EG and bulk MoS_2 was performed (Figure S4). The resulting lattice constants of MoS_2/EG and bulk MoS_2 are 3.160 ± 0.005 and 3.159 ± 0.006

Å, which indicate a relaxed in-plane structure of MoS_2 on EG similar to its bulk counterpart. The lack of in-plane strain in the synthesized MoS_2 2D crystals can be explained by total strain relaxation in the van der Waals gap, analogous to a buffer layer alleviating the strain in conventional epitaxy.[62]

As indicated by the red MoS_2 triangles in Figure 1d, there is a secondary, less preferred registration between MoS_2 and EG, where the MoS_2 lattice is rotated by 30°. To examine the relative amount of 30° rotated growth, GIWAXS data of the $MoS_2(010)$ peak taken along the EG[010] direction (aligned growth, blue) and the SiC[010] direction (30° rotated growth, red) are shown in Figure 7. From the integrated intensities of the two MoS_2 peaks, the amount of MoS_2 with lattice 30° rotated from the EG lattice is determined to be $14 \pm 4\%$ of the total intensities, while the aligned growth is found to be dominant at $86 \pm 4\%$. This large-area GIWAXS result is consistent with the orientation distribution of MoS_2 domains
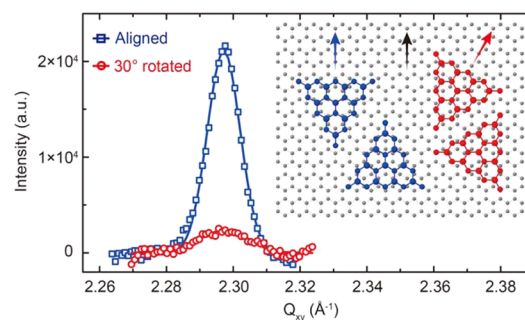

Figure 7. Examination of the growth orientation of MoS_2. GIWAXS data of the $MoS_2(010)$ peak taken along the EG[010] direction (aligned growth, blue) and the SiC[010] direction (30° rotated growth, red). The integrated intensities of these two peaks are 2.6×10^5 and 4.2×10^4, respectively. Inset: Schematic of the two growth orientations of MoS_2 on EG. The armchair directions of MoS_2 from aligned (blue) and 30° rotated (red) growth are indicated by the blue and red arrows, respectively. The black arrow indicates the armchair direction of EG.

shown in the AFM images in Figures 1 and S1. Thus, in Figure 1d, we attribute the majority blue MoS_2 triangles to aligned growth, and the minority red triangles to 30° rotated growth. The inset of Figure 7 shows the schematic of these two registrations, where the blue, black, and red arrows indicate the armchair directions of aligned MoS_2, EG, and 30° rotated MoS_2, respectively. These two growth orientations have also been observed previously for MoS_2 grown on sapphire.[61,63] Rare deviations in the preferred orientations, such as the pink MoS_2 crystal domain shown in Figure 1d, indicate lack of registry of the MoS_2 domain with the EG and can be attributed to local disturbances in the substrate surface. These occurrences were not frequent enough to produce detectable scattered X-ray intensity.

CONCLUSIONS

In summary, a 2D heterostructure of rotationally commensurate MoS_2 on EG has been grown *via* van der Waals epitaxy with controlled thickness. The structural and electronic quality of these samples has been probed down to the atomic scale using a combination of UHV STM/STS and synchrotron X-ray scattering. MoS_2 is found to preferentially grow with lattice aligned with EG. The relative amount of a less preferred 30° rotated growth is also determined. Furthermore, Raman spectroscopy and in-plane X-ray diffraction show that the MoS_2 is nearly strain-free, thus providing an ideal system for probing the fundamental properties of two-dimensional MoS_2. For example, spatially resolved STS measurements across MoS_2 step edges reveal band gap narrowing that is in close agreement with DFT calculations. Overall, this study suggests that EG may be a promising substrate for van der Waals epitaxial growth of other emerging two-dimensional nanomaterials in addition to providing a well-defined platform for the future study and application of MoS_2/graphene heterostructures.

METHODS

Synthesis of Epitaxial Graphene. Following a similar procedure of producing EG on 6H-SiC (0001) as outlined previously,[15,16] an n-type 4H-SiC (0001) wafer (Cree Inc.) degreased in an acetone and isopropyl alcohol (IPA) sonication bath was degassed at 550 °C for 12 h under UHV conditions (~5×10^{-10} Torr). Few-layer EG was grown on the Si face by thermal desorption of Si atoms at 1270 °C for 20 min. The first carbon-rich buffer layer has a $6\sqrt{3} \times 6\sqrt{3}$ unit cell, which is known as the $(6\sqrt{3} \times 6\sqrt{3})R30°$ reconstruction.

Synthesis of MoS_2. Molybdenum trioxide (MoO_3, 99.98% trace metal Sigma-Aldrich) was placed in the middle of the hot zone of a Lindberg/Blue 1 in. quartz tube furnace in an alumina boat 2.5 cm upstream of a 5 mm × 9 mm EG substrate (graphitized Si face is facing up). The sulfur powder (Sigma-Aldrich) in an alumina boat was placed 30 cm upstream of the MoO_3 boat under a proportional integral derivative temperature-controlled heating belt. The tube was initially pumped to a base pressure of ~50 mTorr and purged with Ar gas to 400 Torr. During the anneal prior to the reaction and during the reaction itself, the pressure was kept constant at 43 Torr (to yield mostly monolayer MoS_2 crystals) using a needle valve controller and Ar carrier gas flowing at 25 sccm. The MoO_3 and EG substrate were annealed for 20 min at 150 °C (with a 5 min ramp to 150 °C from room temperature) to eliminate residual water and physisorbed contaminants in the tube and on the substrate. Subsequently, the furnace was heated to a maximum temperature of 800 °C at a rate of 12 °C/min. Once the target temperature was reached, the furnace was kept at 800 °C for 20 min and cooled down naturally to room temperature. Concurrently, the sulfur was annealed under the same inert conditions for 49 min at 50 °C (with 5 min ramp to 50 °C from room temperature) and brought to a maximum temperature of 140 °C

at a rate of 4 °C/min. The sulfur ramp to 140 °C began when the furnace was approximately at 500 °C. The sulfur was then kept at the maximum temperature for 23 min.

For the synthesis of MoS_2 on SiO_2, a 4 cm × 1 cm 300 nm thick SiO_2/Si wafer (SQI Inc.) was sonicated in acetone and IPA bath for 10 min, rinsed with deionized water, and treated with oxygen plasma for 1 min. The wafer was then placed in close proximity to the MoO_3 boat, and the same growth procedure was applied with a change to the following parameters: a reaction chamber pressure of 150 Torr was maintained instead of 43 Torr, and the sulfur was brought to a maximum temperature of 150 °C instead of 140 °C at a rate of 4.5 °C/min.

Scanning Tunneling Microscopy and Spectroscopy. A home-built UHV STM system[54] integrated with a preparation chamber, an XPS chamber, and a load lock was utilized for STM, STS, and XPS measurements. The microscope adopts a Lyding design[64] with a bias voltage applied to the sample with respect to the grounded tip. The base pressure in the STM chamber was ~6×10^{-11} Torr. Both electrochemically etched W and PtIr tips (Keysight) were used. STS spectra and mappings were taken with a lock-in amplifier (SRS model SR850) with a modulation frequency of ~8.5 kHz and rms amplitude of 30 mV. The experimental variability of band gap measurements in this work is estimated to be 0.08 eV. This estimate is based on the standard deviation of band gap measurements (Figure S5) from 80 STS spectra on multiple monolayer MoS_2 domains. Specifically, these measurements imply that the band gap is 2.01 ± 0.08 eV. Nanonis SPM control electronics were used for data collection. The STM system was calibrated using atomic resolution EG for the $x-y$ piezo and Ag(111) single-crystal monolayer step height for the z piezo.

Atomic Force Microscopy. AFM experiments were carried out on an Asylum Cypher AFM in tapping and contact modes. Si cantilevers NCHR-W from NanoWorld with a resonant frequency of ~320 kHz were used for tapping mode imaging, and PPP-CONTSCAu cantilevers from NanoSensors were used for contact mode imaging (2−5 nN force was applied). The images were taken with a pixel resolution of 512 × 512 or 1024 × 1024 at a scanning rate of ~1 Hz.

X-ray Photoelectron Spectroscopy. XPS spectra were taken at a base pressure of ~4×10^{-10} Torr with an Omicron DAR 400 M X-ray source, XM 500 X-ray monochromator, and EA 125 energy analyzer. The XPS system was integrated with the UHV STM system for *in situ* measurements. The binding energy resolution was 0.1 eV. Ten scans were averaged for each core level spectrum. All subpeaks were fit with a modified Shirley background in Avantage (Thermo Scientific) software after calibrating the spectra to graphene carbon at 284.5 eV. The peaks positions are as follow: S 2s, 227.0 eV; MoS_2 $3d_{5/2}$, 229.7 eV; MoS_2 $3d_{3/2}$, 232.8 eV; MoO_x $3d_{5/2}$, 233.1 eV; and MoO_x $3d_{3/2}$, 236.3 eV.

Raman Spectroscopy. Raman measurements were carried out on a Horiba Scientific XploRA PLUS Raman microscope with excitation laser line of 532 nm (with spot size ~1 μm^2) in ambient conditions. The Raman signal was collected using a 100× Olympus objective (NA = 0.9) and dispersed by 1800 grooves/mm grating to a Syncerity CCD detector with a corresponding spectral resolution finer than 2 cm^{-1}. A laser power of about 1 mW was used with an acquisition time of ~15 s to avoid heating effects. The Raman spectra were collected in the spatial mapping mode with step sizes of ~500 nm. The MoS_2 Raman modes of E^1_{2g} and A_{1g} on both the EG/4H-SiC and SiO_2/Si substrates were fitted with Lorentzian functions and calibrated against the 4H-SiC band[65] at 776.65 cm^{-1} and Si band at 520.7 cm^{-1}, respectively.

Synchrotron X-ray Scattering. The GIWAXS data of MoS_2/EG/SiC were collected at sector 12-ID-C at the Argonne National Laboratory Advanced Photon Source. The 23.5 keV monochromatic X-ray beam was defined using slits of 50 μm × 2 mm to have a 5 mm × 2 mm footprint on the sample at incident angle α = 0.14°. The incident flux was 4×10^{12} photons/s. As depicted in Figure 6a, a 100 K Pilatus area detector was mounted on a rotating ν-arm positioned at approximately 354 mm from the sample to collect the GIWAXS signal. Data within q = 2.2 to 4.8 $Å^{-1}$ in Figure 6 was collected at ν = 10.262° relative to the direct beam. The sample was kept under a helium

environment and placed on a ϕ rotation stage. The 33-ID-C line was used to collect high-resolution grazing-incidence X-ray scattering and diffraction data from the bulk MoS_2 single crystal and MoS_2/EG samples. Monochromatic 10 keV X-rays were focused to 70 μm × 30 μm using a horizontal Kirkpatrick-Baez mirror with a flux of 2×10^{11} photons/s. Data were collected using a Dectris 100 K Pilatus area detector mounted on a Newport 6-circle goniometer. The reciprocal space map in Figure 6b was generated using the Ewald sphere construction method, wherein pixels from $Q_z = 0.08$ to 0.12 Å^{-1} were projected onto a 2D reciprocal space map using interpolation plots in Mathematica. Peaks were fit using the Gaussian fitting function in MATLAB.

ASSOCIATED CONTENT

Ⓢ Supporting Information

The Supporting Information is available free of charge on the ACS Publications website at DOI: 10.1021/acsnano.5b06398.

> Additional information including supplemental AFM, STM/STS, optical images, and lattice constants analysis (PDF)

AUTHOR INFORMATION

Corresponding Authors
*E-mail: bedzyk@northwestern.edu.
*E-mail: m-hersam@northwestern.edu.

Author Contributions
¶X.L. and I.B. contributed equally.

Notes
The authors declare no competing financial interest.

REFERENCES

(1) Reina, A.; Jia, X.; Ho, J.; Nezich, D.; Son, H.; Bulovic, V.; Dresselhaus, M. S.; Kong, J. Large Area, Few-Layer Graphene Films on Arbitrary Substrates by Chemical Vapor Deposition. *Nano Lett.* **2009**, 9, 30−35.

(2) Emery, J. D.; Wheeler, V. H.; Johns, J. E.; McBriarty, M. E.; Detlefs, B.; Hersam, M. C.; Gaskill, D. K.; Bedzyk, M. J. Structural Consequences of Hydrogen Intercalation of Epitaxial Graphene on SiC(0001). *Appl. Phys. Lett.* **2014**, 105, 161602.

(3) Song, L.; Ci, L.; Lu, H.; Sorokin, P. B.; Jin, C.; Ni, J.; Kvashnin, A. G.; Kvashnin, D. G.; Lou, J.; Yakobson, B. I.; et al. Large Scale Growth and Characterization of Atomic Hexagonal Boron Nitride Layers. *Nano Lett.* **2010**, 10, 3209−3215.

(4) Zhang, H.; Liu, C.-X.; Qi, X.-L.; Dai, X.; Fang, Z.; Zhang, S.-C. Topological Insulators in Bi_2Se_3, Bi_2Te_3 and Sb_2Te_3 with a Single Dirac Cone on the Surface. *Nat. Phys.* **2009**, 5, 438−442.

(5) Wood, J. D.; Wells, S. A.; Jariwala, D.; Chen, K.-S.; Cho, E.; Sangwan, V. K.; Liu, X.; Lauhon, L. J.; Marks, T. J.; Hersam, M. C. Effective Passivation of Exfoliated Black Phosphorus Transistors Against Ambient Degradation. *Nano Lett.* **2014**, 14, 6964−6970.

(6) Liu, X.; Wood, J. D.; Chen, K.-S.; Cho, E.; Hersam, M. C. In Situ Thermal Decomposition of Exfoliated Two-Dimensional Black Phosphorus. *J. Phys. Chem. Lett.* **2015**, 6, 773−778.

(7) Kang, J.; Wood, J. D.; Wells, S. A.; Lee, J.-H.; Liu, X.; Chen, K.-S.; Hersam, M. C. Solvent Exfoliation of Electronic-Grade, Two-Dimensional Black Phosphorus. *ACS Nano* **2015**, 9, 3596−3604.

(8) Kang, J.; Seo, J.-W. T.; Alducin, D.; Ponce, A.; Yacaman, M. J.; Hersam, M. C. Thickness Sorting of Two-Dimensional Transition Metal Dichalcogenides *via* Copolymer-Assisted Density Gradient Ultracentrifugation. *Nat. Commun.* **2014**, 5, 5478.

(9) Zhang, C.; Johnson, A.; Hsu, C.-L.; Li, L.-J.; Shih, C.-K. Direct Imaging of Band Profile in Single Layer MoS_2 on Graphite: Quasiparticle Energy Gap, Metallic Edge States, and Edge Band Bending. *Nano Lett.* **2014**, 14, 2443−2447.

(10) Shi, Y.; Zhou, W.; Lu, A.-Y.; Fang, W.; Lee, Y.-H.; Hsu, A. L.; Kim, S. M.; Kim, K. K.; Yang, H. Y.; Li, L.-J.; et al. Van der Waals Epitaxy of MoS_2 Layers Using Graphene as Growth Templates. *Nano Lett.* **2012**, 12, 2784−2791.

(11) Yu, L.; Lee, Y.-H.; Ling, X.; Santos, E. J. G.; Shin, Y. C.; Lin, Y.; Dubey, M.; Kaxiras, E.; Kong, J.; Wang, H.; et al. Graphene/MoS_2 Hybrid Technology for Large-Scale Two-Dimensional Electronics. *Nano Lett.* **2014**, 14, 3055−3063.

(12) Roy, K.; Padmanabhan, M.; Goswami, S.; Sai, T. P.; Ramalingam, G.; Raghavan, S.; Ghosh, A. Graphene-MoS_2 Hybrid Structures for Multifunctional Photoresponsive Memory Devices. *Nat. Nanotechnol.* **2013**, 8, 826−830.

(13) Li, Y.; Wang, H.; Xie, L.; Liang, Y.; Hong, G.; Dai, H. MoS_2 Nanoparticles Grown on Graphene: An Advanced Catalyst for the Hydrogen Evolution Reaction. *J. Am. Chem. Soc.* **2011**, 133, 7296−7299.

(14) Chang, K.; Chen, W. L-Cysteine-Assisted Synthesis of Layered MoS_2/Graphene Composites with Excellent Electrochemical Performances for Lithium Ion Batteries. *ACS Nano* **2011**, 5, 4720−4728.

(15) Alaboson, J. M. P.; Wang, Q. H.; Emery, J. D.; Lipson, A. L.; Bedzyk, M. J.; Elam, J. W.; Pellin, M. J.; Hersam, M. C. Seeding Atomic Layer Deposition of High-k Dielectrics on Epitaxial Graphene with Organic Self-Assembled Monolayers. *ACS Nano* **2011**, 5, 5223−5232.

(16) Karmel, H. J.; Garramone, J. J.; Emery, J. D.; Kewalramani, S.; Bedzyk, M. J.; Hersam, M. C. Self-Assembled Organic Monolayers on Epitaxial Graphene with Enhanced Structural and Thermal Stability. *Chem. Commun.* **2014**, 50, 8852−8855.

(17) Emtsev, K. V.; Bostwick, A.; Horn, K.; Jobst, J.; Kellogg, G. L.; Ley, L.; McChesney, J. L.; Ohta, T.; Reshanov, S. A.; Röhrl, J.; et al. Towards Wafer-Size Graphene Layers by Atmospheric Pressure Graphitization of Silicon Carbide. *Nat. Mater.* **2009**, 8, 203−207.

(18) Çelebi, C.; Yanık, C.; Demirkol, A. G.; Kaya, İ. İ. The Effect of a SiC Cap on the Growth of Epitaxial Graphene on SiC in Ultra High Vacuum. *Carbon* **2012**, 50, 3026−3031.

(19) Norimatsu, W.; Kusunoki, M. Transitional Structures of the Interface Between Graphene and 6H−SiC (0001). *Chem. Phys. Lett.* **2009**, 468, 52−56.

(20) Tanabe, S.; Sekine, Y.; Kageshima, H.; Nagase, M.; Hibino, H. Carrier Transport Mechanism in Graphene on SiC(0001). *Phys. Rev. B: Condens. Matter Mater. Phys.* **2011**, 84, 115458.

(21) Jobst, J.; Waldmann, D.; Speck, F.; Hirner, R.; Maude, D. K.; Seyller, T.; Weber, H. B. Quantum Oscillations and Quantum Hall Effect in Epitaxial Graphene. *Phys. Rev. B: Condens. Matter Mater. Phys.* **2010**, 81, 195434.

(22) Riedl, C.; Coletti, C.; Iwasaki, T.; Zakharov, A. A.; Starke, U. Quasi-Free-Standing Epitaxial Graphene on SiC Obtained by Hydrogen Intercalation. *Phys. Rev. Lett.* **2009**, 103, 246804.

(23) Fukidome, H.; Kawai, Y.; Fromm, F.; Kotsugi, M.; Handa, H.; Ide, T.; Ohkouchi, T.; Miyashita, H.; Enta, Y.; Kinoshita, T.; et al. Precise Control of Epitaxy of Graphene by Microfabricating SiC Substrate. *Appl. Phys. Lett.* **2012**, *101*, 041605.

(24) Eriksson, J.; Pearce, R.; Iakimov, T.; Virojanadara, C.; Gogova, D.; Andersson, M.; Syväjärvi, M.; Lloyd Spetz, A.; Yakimova, R. The Influence of Substrate Morphology on Thickness Uniformity and Unintentional Doping of Epitaxial Graphene on SiC. *Appl. Phys. Lett.* **2012**, *100*, 241607.

(25) Ugeda, M. M.; Bradley, A. J.; Shi, S.-F.; da Jornada, F. H.; Zhang, Y.; Qiu, D. Y.; Ruan, W.; Mo, S.-K.; Hussain, Z.; Shen, Z.-X.; et al. Giant Bandgap Renormalization and Excitonic Effects in a Monolayer Transition Metal Dichalcogenide Semiconductor. *Nat. Mater.* **2014**, *13*, 1091−1095.

(26) Zhang, Y.; Chang, T.-R.; Zhou, B.; Cui, Y.-T.; Yan, H.; Liu, Z.; Schmitt, F.; Lee, J.; Moore, R.; Chen, Y.; et al. Direct Observation of the Transition from Indirect to Direct Bandgap in Atomically Thin Epitaxial MoSe₂. *Nat. Nanotechnol.* **2013**, *9*, 111−115.

(27) Huang, Y. L.; Chen, Y.; Zhang, W.; Quek, S. Y.; Chen, C.-H.; Li, L.-J.; Hsu, W.-T.; Chang, W.-H.; Zheng, Y. J.; Chen, W.; et al. Bandgap Tunability at Single-Layer Molybdenum Disulphide Grain Boundaries. *Nat. Commun.* **2015**, *6*, 6298.

(28) Lu, C.-I.; Butler, C. J.; Huang, J.-K.; Hsing, C.-R.; Yang, H.-H.; Chu, Y.-H.; Luo, C.-H.; Sun, Y.-C.; Hsu, S.-H.; Yang, K.-H. O.; et al. Graphite Edge Controlled Registration of Monolayer MoS₂ Crystal Orientation. *Appl. Phys. Lett.* **2015**, *106*, 181904.

(29) Lin, Y.-C.; Lu, N.; Perea-Lopez, N.; Li, J.; Lin, Z.; Peng, X.; Lee, C. H.; Sun, C.; Calderin, L.; Browning, P. N.; et al. Direct Synthesis of van der Waals Solids. *ACS Nano* **2014**, *8*, 3715−3723.

(30) Miwa, J. A.; Dendzik, M.; Grønborg, S. S.; Bianchi, M.; Lauritsen, J. V.; Hofmann, P.; Ulstrup, S. Van der Waals Epitaxy of Two-Dimensional MoS₂-Graphene Heterostructures in a Ultra-High Vacuum. *ACS Nano* **2015**, *9*, 6502−6510.

(31) Koma, A.; Yoshimura, K. Ultrasharp Interfaces Grown with van der Waals Epitaxy. *Surf. Sci.* **1986**, *174*, 556−560.

(32) Koma, A. Van der Waals Epitaxy for Highly Lattice-Mismatched Systems. *J. Cryst. Growth* **1999**, *201-202*, 236−241.

(33) Jiang, J.-W.; Zhuang, X.; Rabczuk, T. Orientation Dependent Thermal Conductance in Single-Layer MoS₂. *Sci. Rep.* **2013**, *3*, 2209.

(34) van der Zande, A. M. Grains and Grain Boundaries in Highly Crystalline Monolayer Molybdenum Disulphide. *Nat. Mater.* **2013**, *12*, 554−561.

(35) Sangwan, V. K.; Jariwala, D.; Kim, I. S.; Chen, K.-S.; Marks, T. J.; Lauhon, L. J.; Hersam, M. C. Gate-Tunable Memristive Phenomena Mediated by Grain Boundaries in Single-Layer MoS₂. *Nat. Nanotechnol.* **2015**, *10*, 403−406.

(36) Rutter, G. M.; Crain, J. N.; Guisinger, N. P.; Li, T.; First, P. N.; Stroscio, J. A. Scattering and Interference in Epitaxial Graphene. *Science* **2007**, *317*, 219−222.

(37) Cockayne, E.; Rutter, G. M.; Guisinger, N. P.; Crain, J. N.; First, P. N.; Stroscio, J. A. Grain Boundary Loops in Graphene. *Phys. Rev. B: Condens. Matter Mater. Phys.* **2011**, *83*, 195425.

(38) Lopez-Sanchez, O.; Lembke, D.; Kayci, M.; Radenovic, A.; Kis, A. Ultrasensitive Photodetectors Based on Monolayer MoS₂. *Nat. Nanotechnol.* **2013**, *8*, 497−501.

(39) Poon, S. W.; Chen, W.; Wee, A. T. S.; Tok, E. S. Growth Dynamics and Kinetics of Monolayer and Multilayer Graphene on a 6H-SiC(0001) Substrate. *Phys. Chem. Chem. Phys.* **2010**, *12*, 13522−13533.

(40) Zhang, Y.; Fu, Q.; Cui, Y.; Mu, R.; Jin, L.; Bao, X. Enhanced Reactivity of Graphene Wrinkles and Their Function as Nanosized Gas Inlets for Reactions Under Graphene. *Phys. Chem. Chem. Phys.* **2013**, *15*, 19042−19048.

(41) Kim, K. K.; Reina, A.; Shi, Y.; Park, H.; Li, L.-J.; Lee, Y. H.; Kong, J. Enhancing the Conductivity of Transparent Graphene Films *via* Doping. *Nanotechnology* **2010**, *21*, 285205.

(42) Sharma, R.; Baik, J. H.; Perera, C. J.; Strano, M. S. Anomalously Large Reactivity of Single Graphene Layers and Edges Toward Electron Transfer Chemistries. *Nano Lett.* **2010**, *10*, 398−405.

(43) Hansen, L. P.; Johnson, E.; Brorson, M.; Helveg, S. Growth Mechanism for Single- and Multi-Layer MoS₂ Nanocrystals. *J. Phys. Chem. C* **2014**, *118*, 22768−22773.

(44) Cheng, Y.; Yao, K.; Yang, Y.; Li, L.; Yao, Y.; Wang, Q.; Zhang, X.; Han, Y.; Schwingenschlögl, U. Van der Waals Epitaxial Growth of MoS₂ on SiO₂/Si by Chemical Vapor Deposition. *RSC Adv.* **2013**, *3*, 17287−17293.

(45) Lee, C.; Yan, H.; Brus, L. E.; Heinz, T. F.; Hone, J.; Ryu, S. Anomalous Lattice Vibrations of Single- and Few-Layer MoS₂. *ACS Nano* **2010**, *4*, 2695−2700.

(46) Hui, Y. Y.; Liu, X.; Jie, W.; Chan, N. Y.; Hao, J.; Hsu, Y.-T.; Li, L.-J.; Guo, W.; Lau, S. P. Exceptional Tunability of Band Energy in a Compressively Strained Trilayer MoS₂ Sheet. *ACS Nano* **2013**, *7*, 7126−7131.

(47) Chakraborty, B.; Bera, A.; Muthu, D. V. S.; Bhowmick, S.; Waghmare, U. V.; Sood, A. K. Symmetry-Dependent Phonon Renormalization in Monolayer MoS₂ transistor. *Phys. Rev. B: Condens. Matter Mater. Phys.* **2012**, *85*, 161403.

(48) Lee, J. E.; Ahn, G.; Shim, J.; Lee, Y. S.; Ryu, S. Optical Separation of Mechanical Strain from Charge Doping in Graphene. *Nat. Commun.* **2012**, *3*, 1024.

(49) Rice, C.; Young, R. J.; Zan, R.; Bangert, U.; Wolverson, D.; Georgiou, T.; Jalil, R.; Novoselov, K. S. Raman-Scattering Measurements and First-Principles Calculations of Strain-Induced Phonon Shifts in Monolayer MoS₂. *Phys. Rev. B: Condens. Matter Mater. Phys.* **2013**, *87*, 081307.

(50) Castellanos-Gomez, A.; Roldán, R.; Cappelluti, E.; Buscema, M.; Guinea, F.; van der Zant, H. S. J.; Steele, G. A. Local Strain Engineering in Atomically Thin MoS₂. *Nano Lett.* **2013**, *13*, 5361−5366.

(51) Bernardi, M.; Palummo, M.; Grossman, J. C. Extraordinary Sunlight Absorption and One Nanometer Thick Photovoltaics Using Two-Dimensional Monolayer Materials. *Nano Lett.* **2013**, *13*, 3664−3670.

(52) Dolui, K.; Rungger, I.; Sanvito, S. Origin of the *n*-Type and *p*-Type Conductivity of MoS₂ monolayers on a SiO₂ substrate. *Phys. Rev. B: Condens. Matter Mater. Phys.* **2013**, *87*, 165402.

(53) Liu, Z.; Amani, M.; Najmaei, S.; Xu, Q.; Zou, X.; Zhou, W.; Yu, T.; Qiu, C.; Birdwell, A. G.; Crowne, F. J.; et al. Strain and Structure Heterogeneity in MoS₂ Atomic Layers Grown by Chemical Vapour Deposition. *Nat. Commun.* **2014**, *5*, 5246.

(54) Foley, E. T.; Yoder, N. L.; Guisinger, N. P.; Hersam, M. C. Cryogenic Variable Temperature Ultrahigh Vacuum Scanning Tunneling Microscope for Single Molecule Studies on Silicon Surfaces. *Rev. Sci. Instrum.* **2004**, *75*, 5280−5287.

(55) Chen, C. J. *Introduction to Scanning Tunneling Microscopy*; Oxford University Press: New York, 1993; pp 196−198.

(56) Maroutian, T.; Degen, S.; Becker, C.; Wandelt, K.; Berndt, R. Superstructures and Coincidences of a Thin Oxide Film on a Metallic Substrate: A STM Study. *Phys. Rev. B: Condens. Matter Mater. Phys.* **2003**, *68*, 155414.

(57) Li, T.; Galli, G. Electronic Properties of MoS₂ Nanoparticles. *J. Phys. Chem. C* **2007**, *111*, 16192−16196.

(58) Bollinger, M. V.; Lauritsen, J. V.; Jacobsen, K. W.; Nørskov, J. K.; Helveg, S.; Besenbacher, F. One-Dimensional Metallic Edge States in MoS₂. *Phys. Rev. Lett.* **2001**, *87*, 196803.

(59) Dong, L.; Wang, J.; Namburu, R.; O'Regan, T. P.; Dubey, M.; Dongare, A. M. Edge Effects on Band Gap Energy in Bilayer 2H-MoS₂ Under Uniaxial Strain. *J. Appl. Phys.* **2015**, *117*, 244303.

(60) Van Bommel, A. J.; Crombeen, J. E.; Van Tooren, A. LEED and Auger Electron Observations of the SiC(0001) Surface. *Surf. Sci.* **1975**, *48*, 463−472.

(61) Ji, Q.; Kan, M.; Zhang, Y.; Guo, Y.; Ma, D.; Shi, J.; Sun, Q.; Chen, Q.; Zhang, Y.; Liu, Z. Unravelling Orientation Distribution and Merging Behavior of Monolayer MoS₂ Domains on Sapphire. *Nano Lett.* **2015**, *15*, 198−205.

(62) Bakti Utama, M. I.; Zhang, Q.; Zhang, J.; Yuan, Y.; Belarre, F. J.; Arbiol, J.; Xiong, Q. Recent Developments and Future Directions in

the Growth of Nanostructures by van der Waals Epitaxy. *Nanoscale* **2013**, *5*, 3570−3588.

(63) Dumcenco, D.; Ovchinnikov, D.; Marinov, K.; Lazić, P.; Gibertini, M.; Marzari, N.; Sanchez, O. L.; Kung, Y.-C.; Krasnozhon, D.; Chen, M.-W.; et al. Large-Area Epitaxial Monolayer MoS$_2$. *ACS Nano* **2015**, *9*, 4611−4620.

(64) Brockenbrough, R. T.; Lyding, J. W. Inertial Tip Translator for a Scanning Tunneling Microscope. *Rev. Sci. Instrum.* **1993**, *64*, 2225−2228.

(65) Lin, S.; Chen, Z.; Li, L.; Yang, C. Effect of Impurities on the Raman Scattering of 6H-SiC Crystals. *Mater. Res.* **2012**, *15*, 833−836.